Turbulence numerical simulation of flow characteristics of Laval nozzle top blow jet

Ai-liang CHEN[1], Yao LIU[1], Zi-biao WANG[1], Huan-wu ZHAN[2],
Xue-xian JIANG[3], Feng-long SUN[1], Jiann-yang HWANG[4], Xi-jun ZHANG[5]

1. School of Metallurgy and Environment, Central South University, Changsha 410083, China;
2. Guangxi Nanguo Copper Co., Ltd., Nandan 547204, China;
3. Department of Metallurgical and Resource Engineering, Guilin University of Technology at Nanning,
Nanning 530001, China;
4. Department of Materials Science and Engineering, Michigan Technological University, Houghton, MI 49931, USA;
5. State Key Laboratory of Comprehensive Utilization of Nickel and Cobalt Resources,
Jinchuan Group Co., Ltd., Jinchang 737100, China

Abstract: The turbulent characteristics of the top-blown Laval nozzle and the influence of pressure and Mach number were studied through numerical simulation. With 2.72% error between the results and the empirical formula, the results are reliable. Nozzle fluid is influenced by pipe structure, causing pressure and density to drop as speed increases. Differences in pressure and velocity between the jet and surrounding gas lead to jet velocity attenuation, flow expansion, deflection, and eddy currents. The optimal top blowing pressure is 0.6 MPa, and the center velocity and width of the jet are 345 m/s and 0.124 m, respectively, at $20D_e$ (D_e is the nozzle exit diameter). It achieves a maximum jet velocity of 456 m/s. The optimal nozzle Mach number is 1.75, with a maximum jet velocity of 451 m/s. At $20D_e$, the jet center velocity is 338 m/s, with a width of 0.12 m.

Key words: top blow jet; numerical simulation; turbulence; flow characteristic; Laval nozzle

1 Introduction

Top-blown oxygen lance jetting technology is commonly used in smelting blast furnaces and steelmaking converters in the metallurgical and chemical industries. It refers to the downward injection of high-speed oxygen-enriched airflow from the top of the stove. The reaction with the furnace material accelerates the heat exchange and material transfer in the furnace [1], promoting combustion and smelting reactions and achieving efficient melting. It has become one of the indispensable critical technologies in the modern metallurgical industry [2]. A deep understanding of the jet characteristics helps to understand the basic principles of gas–liquid interaction. It optimizes the spray devices and gas flow control systems of the production furnace, improving the smelting efficiency and reducing the wear of the furnace wall [3]. It also provides an essential basis and reference for further exploring complex phenomena such as multiphase flow and chemical reactions in the furnace [4].

However, the top-blowing process is affected by coupling complex phenomena in the furnace environment, such as high temperature and chemical reactions [5]. This makes it challenging to

obtain comprehensive and accurate data through experimental methods. By establishing the mathematical and physical models, numerical simulation technology can effectively predict the flow of the jet during the top-blowing process [6]. It makes up for the shortcomings of experimental methods and provides an effective means for studying top-blowing jet characteristics [7].

In recent years, some studies have simulated this process. LI et al [8] found that the jet needs sufficient kinetic energy to stir the molten pool material effectively and drive slag movement during the top-blowing smelting process. DERING et al [9] simulated the top-blowing steelmaking process, and proved that the gas sprayed from the top would form a supersonic jet and act on the surface of the molten pool, intensifying the reaction in the impact zone. ZHANG et al [10] established that in the top-bottom blowing converter, the flow rate and momentum of the top-blowing oxygen jet directly affect the shape of the cavity formed when it impacts the molten surface. It involves the refining effect. Hence, the kinetic energy and motion behavior of the top-blowing jet are closely linked to the smelting effect. This needs to be thoroughly investigated for flow characteristics and optimized top-blowing conditions. LI et al [11] found that the jet at high ambient temperatures has a higher velocity and lower density. JIA et al [12] observed that the jet energy increases with increasing top-blowing flow rate. YAO et al [13] investigated the influence of environmental gas components on the jet. It was confirmed that the high-speed region of the plane increases with an increasing fraction of carbon monoxide volume. DONG et al [14] discovered that the length of the jet core area, jet velocity, and radial width increase with increasing environmental temperature. CAO et al [15] identified that longer blowing time can improve the jet impact capacity. LI et al [16] combined hydraulic model experiments and numerical simulations to find that the core area of the spray jet increases with increasing temperature. DONG et al [17] optimized the nozzle diameter and number of PC oxygen guns, effectively improving the jet penetration ability.

Previous studies have analyzed the working process and influencing factors of top-blowing technology. However, there needs to be more research on jet motion characteristics to analyze the working principle of the top-blowing process and how the pressure and nozzle Mach number affect the top blowing effect by affecting the jet characteristics. In this work, computational fluid dynamics is utilized to numerically simulate the jet flow of the top-blown oxygen lance. An appropriate turbulence model is selected to explore the formation mechanism of the jet flow inside the nozzle. The motion of the jet flow ejected from the nozzle, the velocity attenuation process and the action mechanism are investigated. The influence of the top-blowing operating pressure and the nozzle Mach number on the flow characteristics of the jet flow is analyzed and studied.

2 Numerical simulation model

2.1 Numerical assumptions

There are three assumptions: (1) Chemical reactions inside the converter are not considered. (2) Gas is treated as a compressible fluid. (3) All wall surfaces are assumed to be no-slip surfaces and standard wall functions are used.

2.2 Selection of turbulence model

The flow of the top-blown oxygen lance is characterized by turbulent motion. The choice of turbulence model significantly impacts the simulation results of the jet behavior. Turbulence models are commonly used to describe turbulent flows of liquids or gases to predict the behavior of the flow field more accurately.

Common turbulence models include the k-ε-Standard model, k-ε-RNG model, k-ε-Realizable model, k-ω-Standard model, k-ω-SST model, and Spalart−Allmaras model [18]. Among them, the k-ε-Standard model is the most widely used and is suitable for high Reynolds number flow problems [19]. Based on this model, the k-ε-RNG model considers low Reynolds number flow and has a faster calculation speed. The k-ε-Realizable model considers the dissipation and viscosity generated by laminar wave motion [20]. The k-ω-Standard model is suitable for predicting high-speed and robust turbulence flow conditions. The k-ω-SST has been widely used in high-speed turbulent flow and near-wall free flow. Spalart−Allmaras is a single-equation turbulence model with a solid ability to describe the boundary layer and viscous flow regions [21].

In general, different turbulence models have different applicable ranges. The choice should be made based on the relationship between accuracy and computational cost according to actual conditions [22]. The above six turbulence models are selected to simulate the flow of the top-blown oxygen lance more accurately. The jet flow of the oxygen lance is manufactured under the conditions of Mach number (Ma) of 1.75, environmental temperature of 300 K, and operating pressure of 0.53 MPa in the top-blown converter. The simulation results are analyzed and compared.

The distributions of jet velocity obtained by selecting different turbulence models are shown in Fig. 1. It can be seen from Fig. 1(a) that the jet retains a relatively high downward velocity after being ejected from the nozzle. During this process, the flow rate increases and the flow velocity decreases. After flowing downward for a certain period, a vortex structure is formed in the outer area. The jet gradually becomes unstable, exhibiting oscillations and bending. This is consistent with the simulation results of YANG et al [23] and FAHEEM et al [24]. Based on Figs. 1(b, c), the jet moves downward vertically and then rebounds upward after colliding with the wall, neglecting the entrainment effect of the plane on the surrounding gas. From Fig. 1(d), the jet diffuses outward immediately after ejection, oscillating and bending. Figures 1(e, f) fail to describe the downward flow of high-speed fluid and do not capture the phenomenon of interaction between the jet and the surrounding gas.

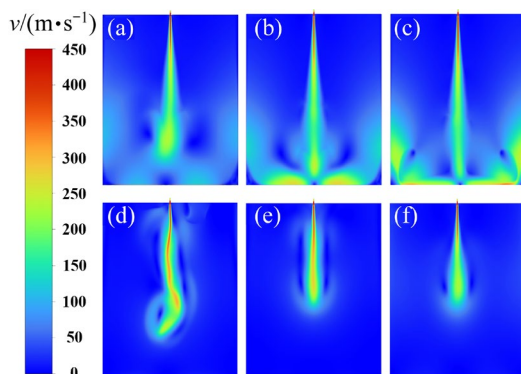To select a suitable turbulence model more accurately, the velocity distribution on the jet center line in the simulation results was compared with the empirical formulas of ERSSON et al [25] and NGUYEN and EVANS [26], and the results are shown in Fig. 2. These studies through experiments on free jets from top-blown oxygen lances, show that at $12D_e$ distance from the nozzle, the velocity attenuation along the central axis of the plane follows a specific pattern. Equations (1) and (2) are proposed to describe the velocity variation along the central axis of the free plane:

$$\frac{U(1)}{U_e} = K_1 \frac{D_e}{x} \tag{1}$$

$$\frac{U(2)}{U_e} = \frac{K_2}{x/D_e + K_3} \tag{2}$$

where $U(1)$ and $U(2)$ are the centerline velocities of the jet corresponding to Eq. (1) and Eq. (2) respectively; U_e is the centerline velocity of the plane at the nozzle exit; K_1, K_2, and K_3 are all constants, taken as 13, 15, and 3.5 respectively; D_e is the nozzle exit diameter; x is the axial distance from the nozzle exit.
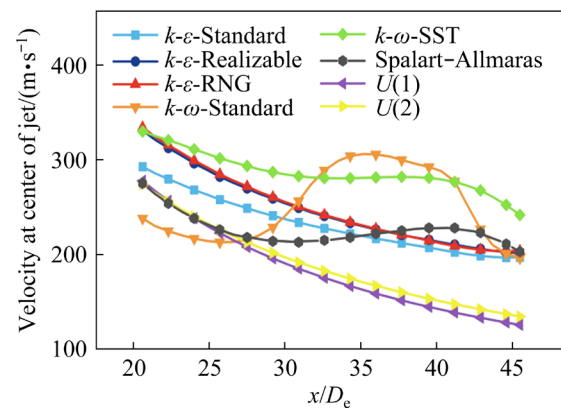

Fig. 2 Velocity at center of jet with different turbulence models

Figure 2 shows that the rules described in Eqs. (1) and (2) are consistent in k-ε-Standard, k-ε-Realizable, k-ε-RNG calculation results. Combined with Fig. 1, k-ε-RNG lacks prediction of vortices and jet instability on both sides of the jet, so k-ε-Standard and k-ε-Realizable are more suitable for the study of this model. By considering the short calculation time of k-ε-Standard, this model is chosen for numerical simulation. In addition, the comparison between the simulation results and the formula can verify the reliability of this model.

Fig. 1 Velocity distribution using different turbulence models: (a) k-ε-Standard model; (b) k-ε-RNG model; (c) k-ε-Realizable model; (d) k-ω-Standard model; (e) k-ω-SST model; (f) Spalart−Allmaras model

2.3 Turbulence model formulation

The k-ε-Standard turbulence model was used, which has become a significant tool in the engineering flow field calculations [27]. Based on the calculation of turbulence kinetic energy and diffusion rate, the k-ε-Standard model adopts a semiempirical formula (the k equation is an exact equation, while the ε equation is an empirical one) [28]. The model assumes that the flow field is entirely turbulent, neglecting intermolecular viscosity. The turbulence kinetic energy equation k and the diffusion equation ε are given by Eqs. (3) and (4), respectively [29]:

$$\frac{\partial(\rho k)}{\partial t}+\frac{\partial(\rho k u)}{\partial x}+\frac{\partial(\rho k v)}{\partial y}+\frac{\partial(\rho k w)}{\partial z}=$$

$$\frac{\partial}{\partial x_j}\left[\left(\mu+\frac{\mu_t}{\sigma_k}\right)\frac{\partial k}{\partial x_j}\right]+G_k-\rho\varepsilon \tag{3}$$

$$\frac{\partial(\rho\varepsilon)}{\partial t}+\frac{\partial(\rho\varepsilon u)}{\partial x}+\frac{\partial(\rho\varepsilon v)}{\partial y}+\frac{\partial(\rho\varepsilon w)}{\partial z}=$$

$$\frac{\partial}{\partial x_j}\left[\left(\mu+\frac{\mu_t}{\sigma_\varepsilon}\right)\frac{\partial\varepsilon}{\partial x_j}\right]+C_{1\varepsilon}\frac{\varepsilon}{k}G_k-C_{2\varepsilon}\rho\frac{\varepsilon^2}{k} \tag{4}$$

where k is the turbulent kinetic energy, ε is the turbulent diffusion rate, t is the time, u, v, and w are the velocity components, ρ is the density, μ is the molecular viscosity, μ_t is the eddy viscosity, and G_k is the turbulence generation term [30]. The model constants involved in the model are set as $C_{1\varepsilon}=1.44$, and $C_{2\varepsilon}=1.92$, which are obtained from basic turbulence experiments of air and water and applied to most cases [31].

2.4 Model geometry and parameters

The simulation model was established based on the field production conditions. The two-dimensional structure of the calculation domain of this research model, the single-hole Laval nozzle used for the top-blown oxygen gun and the main dimensions of them are shown in Fig. 3.

2.5 Grid setting and boundary conditions

Different grid settings were applied to the model and their simulation results were compared. Table 1 gives the amount of the following six mesh distributions. Figures 4 and 5 show the mesh and velocity distribution diagrams under different mesh conditions.
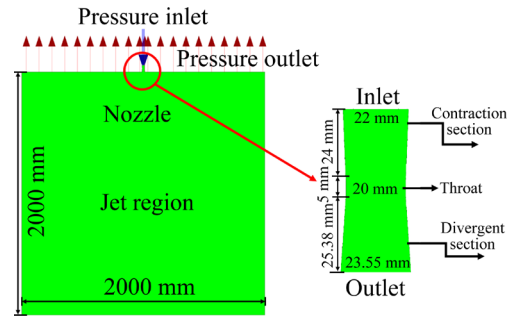

Fig. 3 Two-dimensional computational domain structure diagram

Table 1 Amount of six meshes

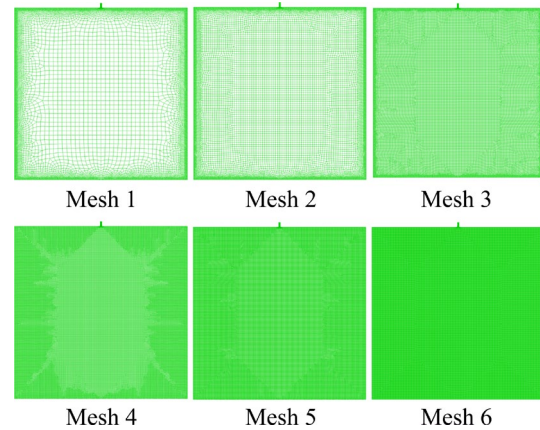| Mesh 1	Mesh 2	Mesh 3	Mesh 4	Mesh 5	Mesh 6
17530	47602	91322	125990	162117	195638

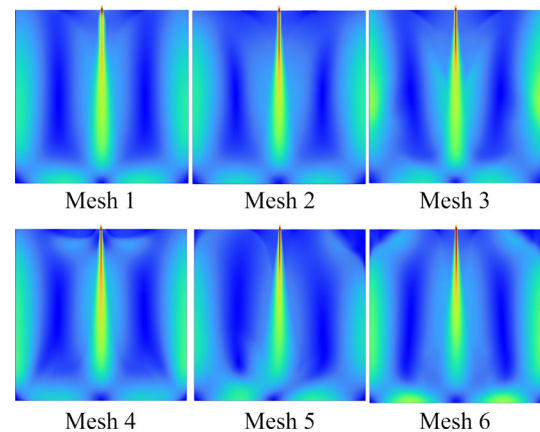**Fig. 4** Mesh distributions under different mesh conditions

Fig. 5 Velocity contours under different mesh conditions

Figure 5 illustrates that different mesh distributions have minimal influence on the overall calculation results, demonstrating the independence of mesh while ensuring uniform convergence in

numerical simulations. However, the smaller the mesh density, the coarser the calculation of details. When the number of mesh is more significant, the transition between the two regions with a more considerable speed difference is better. At the same time, when the mesh is small, the part of the jet diffusion and the vortex formed by the surrounding gas sucked by both sides of the jet cannot be described in detail. This study needs to obtain the flow parameter values of the jet at different positions, so it is better to use a more precise grid for calculation. After considering the calculation result and calculation speed, Mesh 5 was selected for meshing.

The grid quality check revealed that the minimum volume of the model grid was 3.51×10^{-7}, the minimum orthogonal quality was 0.75, and the maximum aspect ratio was 3.73. If the volume of a grid cell is negative, it means that one or more cells have inappropriate connectivity. The model cannot calculate the negative-volume grid. However, all the grid volumes in this study were positive. The calculations could be performed usually. Low-quality grids can cause slow convergence, divergence or nonphysical results [32]. Based on the grid orthogonal quality requirements in Table 2, this study used high-quality grids. The aspect ratio of a grid cell should generally be 10−100. The aspect ratio of the grid cells used in this study met the requirements. In summary, the model grid used in this study has good quality and can achieve relatively accurate simulation results.

This model uses the oxygen gun nozzle inlet as the pressure inlet boundary and the top opening of the jet area as the pressure outlet boundary. Table 3 shows the initial boundary condition parameters of the model.

3 Results and discussion

3.1 Simulation result verification

Some studies have summarized the relationship between the Mach number (Ma) of the nozzle and the diameter of the jet core area by conducting a large number of experiments, and proposed empirical formulas such as Eqs. (5) [33] and (6) [34].

$$L_c/D_e=5+1.78Ma^{2.81} \tag{5}$$

$$L_c/D_e=19.33Ma-17.348Ma^2+6.55Ma^3 \tag{6}$$

where L_c and D_e are the jet core length and the diameter of the nozzle outlet, respectively.

To verify the reliability, the simulation results were compared with the core area length calculation of the empirical formula, as given in Table 4. The results show that the errors between the simulation results and the length of the jet core area obtained by Eqs. (5) and (6) are 2.72% and 6.18%, respectively, which are small, which shows that the simulation results are consistent with the experimental results.

3.2 Flow characteristics of jet under production conditions

The flow characteristics of the top-blown oxygen lance jet were simulated under the production conditions of 0.53 MPa for working pressure and 300 K for ambient temperature with a Ma=1.75 oxygen nozzle. The gas flow inside and outside the nozzle was analyzed and processed based on the simulation results.

As shown in Fig. 6, the air flow inside the nozzle conforms to the one-dimensional isentropic flow law. Under the working condition, the velocity

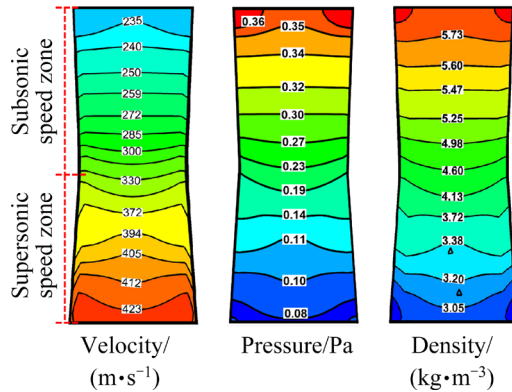**Table 2** Requirements for grid orthogonality quality

Grid quality	Unacceptable	Bad	Acceptable	Good	Very good	Excellent
Minimum orthogonal mass	0−0.001	0.001−0.140	0.15−0.20	0.20−0.69	0.70−0.95	0.95−1.00

Table 3 Boundary conditions of model

Gas physical parameter				Inlet pressure/ MPa	Outlet pressure/ MPa	Temperature/ K
Density	Viscosity/ (kg·m^{-1}·s^{-1})	Specific heat capacity/ (J·kg^{-1}·K^{-1})	Heat conductivity/ (W·m^{-1}·K^{-1})			
Compressible	1.79×10^{-5}	1006.43	0.02	0.53	0.10	293

Table 4 Comparison between simulation results and empirical formula calculation

Simulation result/m	L_c		L_c	
	Eq. (5)/m	Error/%	Eq. (6)/m	Error/%
0.339	0.330	2.72	0.372	6.18

Fig. 6 Distribution of velocity field, pressure field, and density field inside nozzle under operating conditions
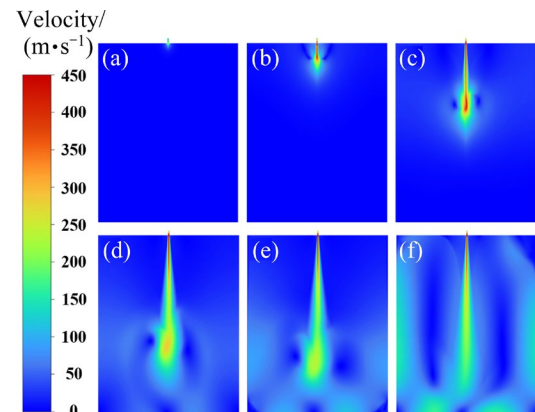
in the nozzle reaches the sound velocity at the throat, the supersonic flow is in the whole expansion section, and the maximum value of 423 m/s is reached at the outlet. Under the influence of the change of the cross-sectional area of the Laval nozzle, the velocity of the flow increases, and the pressure and density of the flow decrease. The pressure decreases from 0.35 to 0.08 MPa, and the density decreases from 5.73 to 3.05 kg/m³.

Figure 7 shows the pressure distribution near the nozzle outlet after the air flows out of the nozzle. The airflow pressure at the nozzle outlet (P_e=0.075 Pa) is lower than the ambient pressure (P_a=0.101 Pa), resulting in an overexpanded flow, and the airflow undergoes compression upon exiting the nozzle. The flow at the nozzle outlet is supersonic, and the pressure outside the nozzle is increased discontinuously due to the sudden compression of the back pressure, which forms a

Fig. 7 Nozzle external pressure distribution

shock wave attached to the outlet section of the expansion section. After the gas passes through the shock wave, the pressure rises to P_a, and then gradually exceeds P_a.

Jet is a phenomenon of high-speed airflow ejected from the nozzle under the action of a pressure difference. The change of its flow state with time is very complicated. Figure 8(a) shows the velocity distribution of the jet at different time points under operating conditions at 0.001 s. The gas flows inside the nozzle under the action of inlet pressure. At 0.01 s, a high-speed airflow is formed at the nozzle outlet and moves downward. The airflow loses its original channel restraint and begins to diffuse to the surrounding air under the resistance of the surrounding air. From 0.03 to 0.10 s, the airflow continues to move downward, and the jet diameter increases. The jet velocity and density decrease but remain high with the diffusion of the jet. Its flow state becomes unstable, forming irregular vortex structures. Its phenomena, such as lateral swing, deflection, bifurcation, and backflow, begin to appear [35]. At 0.20 s, the jet contacts the wall. The velocity and direction change drastically.

Fig. 8 Velocity distribution map at different time intervals under operating conditions: (a) 0.001 s; (b) 0.01 s; (c) 0.03 s; (d) 0.07 s; (e) 0.10 s; (f) 0.20 s

The velocity contour map depicted in Fig. 9 demonstrates a gradient distribution of jet velocity, characterized by a high-speed region located at the center of the jet and a low-speed region at its periphery. The maximum velocity of the jet is 450 m/s, and the jet center velocity and flow width at $20D_e$ are 338 m/s and 0.12 m, respectively. The jet ejected from the nozzle has a cone shape and good linearity and stability. The velocity of the jet in the diffusion zone gradually decreases due to the

significant velocity difference with the surrounding gas, which generates a vast frictional force and sucks in the peripheral gas to form irregular vortices. The surrounding gas flows toward the jet and converges with it, increasing the flow volume [36]. The jet obtains sufficient kinetic energy and volume to jet downward and vigorously stir the material, promoting the reaction. Similarly, the velocity vector distribution map in Fig. 9(b) shows that the jet velocity direction is downward or inclined downward. The flow direction of the surrounding gas is opposite to the jet, which is upward or inclined upward. The formed vortex flows in a circular motion. In the top-blown converter smelting process, the formation and movement of vortices play a crucial role in mixing and stirring the materials in the converter. The size and shape of the vortices can be adjusted by controlling the parameters of the nozzle and airflow to achieve the best mixing effect.
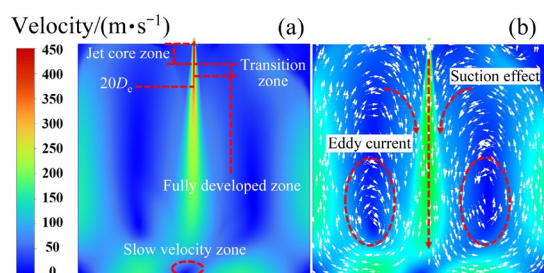

Fig. 9 Velocity contour map (a) and velocity vector distribution (b) of jet flow field

3.3 Influence of operating pressure on jet flow characteristics

The inlet operating pressure of a top-blowing oxygen lance refers to the gas pressure at the nozzle inlet. It is one of the critical parameters affecting the jet performance of the oxygen lance. Changes in operating pressure directly impact the velocity, shape, stability, and range of the jet, consequently influencing the operational efficacy of the top-blown oxygen lance. Based on the numerical simulation of the jet under production conditions, the inlet operating pressure of the oxygen lance was changed to simulate the jet flow under pressure conditions of 0.3, 0.4, 0.6, and 0.7 MPa and compared with the results under the 0.53 MPa, the changes in jet velocity distribution and axial and transverse velocity attenuations were analyzed.

Figure 10 shows the velocity profile of jets

under different inlet operating pressures. The results indicate that when the operating pressure increases from 0.3 to 0.7 MPa, the maximum jet velocity increases from 439 to 471.5 m/s, and the jet stream width at $20D_e$ widens from 0.102 to 0.125 m. The operating pressure also affects the shape of the jet. At lower operating pressures, the jet is in a relatively stable straight line. In comparison, at higher operating pressures, the jet may become bent or twisted, thereby affecting the uniformity and efficiency of the reaction.
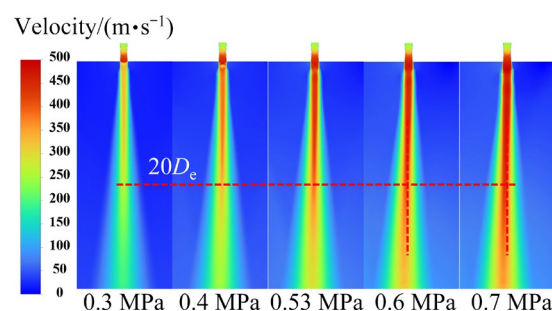

Fig. 10 Velocity profile of jets under different operating pressures

At the outlet of the nozzle ($20D_e$), the jet velocity decays significantly, the flow becomes unstable, and flow is significantly widened. In the top blowing production, the axial distance between the oxygen gun and the melt is about $20D_e$. The fluid flow here is of important research significance, so this section was chosen as the object of follow-up observation. A comparative analysis was carried out on the axial velocity and transverse velocity on the $20D_e$ cross-section of the jet under different operating pressures. The results are shown in Fig. 11.

Figure 11(a) shows that, in general, the attenuation speed of the jet is slower at first and then faster. The velocity of the jet is slow and then fast, relatively stable from 0 to $10D_e$, the fastest at $(10-40)D_e$, and gradually remains stable after $40D_e$. With increasing operating pressure, the jet velocity significantly increases, and the attenuation speed decreases accordingly. When the operating pressure is 0.7 MPa, the velocity attenuation curve on the jet axis is the smoothest, and the core length is approximately $10D_e$. However, the velocity attenuation curves at 0.3 and 0.4 MPa are steeper, and the velocity attenuation is more prominent. This loses a large amount of impact kinetic energy

and is not conducive to the subsequent agitation of the material. Figure 11(b) shows that the jet diffusion radius is approximately 0.06 m on the $20D_e$ cross-section. With the increase in the operating pressure of the top-blown jet, the jet radius decreases, but the degree of decrease is relatively small. This is because the increase in operating pressure causes an increase in the jet velocity. Moreover, the jet encounters increased resistance as it propagates through the air. Meanwhile, the diameter of the nozzle outlet is fixed. When the jet velocity increases, the flow rate also increases. This results in an increase in jet density and a decrease in jet radius.
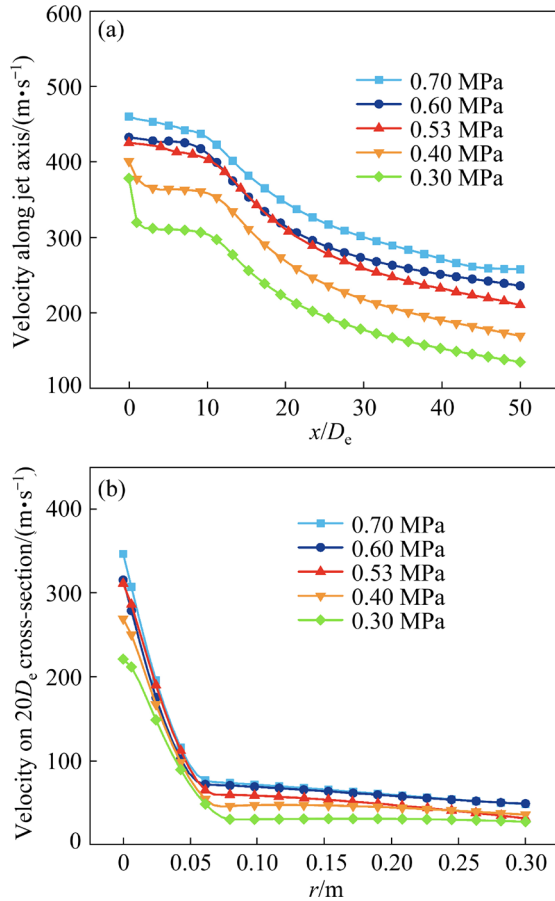

Fig. 11 Velocity distribution along jet axis (a) and on $20D_e$ cross-section (b) under different operating pressures

In conclusion, the increase of operating pressure can significantly increase the jet velocity, reduce the axial and radial velocity decay, broaden the jet flow, so that it has stronger impact kinetic energy and larger impact area. But the excessive operating pressure can cause the jet to become unstable [37], which can affect the uniformity and efficiency of the material reaction. Based on the above analysis, when the operating pressure is 0.6 MPa, the maximum jet velocity is 456 m/s, the jet center velocity and flow width at $20D_e$ are 345 m/s and 0.124 m respectively, and the flow condition is stable, the jet flow formed under this condition is optimal.

Furthermore, with variations in the operational pressure of the oxygen lance, the length of the jet core region also changes. Through top-blowing experiments, TAGO and HIGUCHI [38], and NAITO et al [39], discovered a certain pattern in the alteration of the jet core region length in response to lance pressure variations. They respectively expressed this phenomenon using empirical formulas:

$$L_{c_1}/d_e = 2.47\left(P_0/P^*\right) \tag{7}$$

$$L_{c_2}/d_t = M_o\left(5.88 + 1.54M_o^2\right),$$
$$M_o = \left[5\left\{\left(P_0/P^*\right)^{2/7} - 1\right\}\right]^{1/2} \tag{8}$$

$$L_{c_3}/d_t = 2.24\left(P_0/P^*\right) + 6.16 \tag{9}$$

In order to further investigate the influence of operational pressure on jet motion characteristics, the simulation results were compared with Eqs. (7)−(9), as shown in Fig. 12. It can be observed that the length of the jet core region increases with higher operational pressure, and the simulation results closely align with the calculated results from Eqs. (7)−(9). This further validates the accuracy of the simulation results from this model. A linear regression was performed on the simulation result curve, yielding Eq. (10) with a
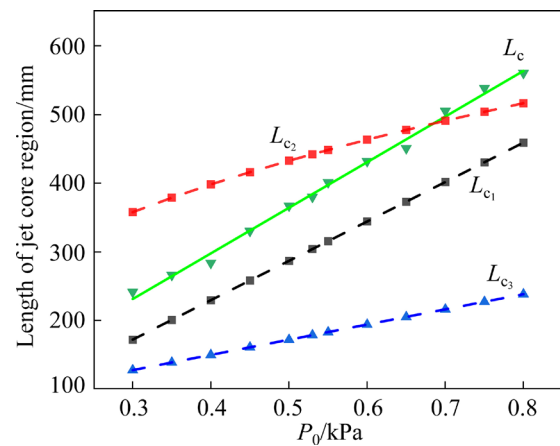

Fig. 12 Variation of length of jet core region with changes in operational pressure

fitted coefficient of determination (R^2) of 0.9946, indicating a robust linear relationship between the length of the jet core region and the operational pressure. The pronounced incline observed in the variation curve of simulation results may be attributed to variations in the geometric structure of the nozzle. Specifically, the slope of the linear relationship between the length of the core region and the operational pressure tends to escalate with higher exit Mach numbers [39]:

$$L_c/d_e = 2.86\left(P_0/P^*\right) + 1.36 \qquad (10)$$

3.4 Influence of jet Mach Number on jet motion characteristics of nozzle

In the top-blowing process, the geometric configuration of the nozzle within the lance governs the flow pattern and velocity distribution of the jet. The size of the nozzle outlet directly impacts the velocity, density, and flow rate of the jet. In the gas dynamics function, distinct ratios of nozzle outlet to throat area correspond to different nozzle outlet Mach numbers. Based on the numerical simulation of jet flow under production conditions, the Mach number of the nozzle of the oxygen gun is changed. The jet flows at Ma=1.25, 1.5, 2, and 2.25 were simulated, and compared with those at Ma=1.75 to analyze the changes in axial and lateral jet velocity distribution and velocity attenuation. Table 5 shows the area ratios of the five nozzle Mach numbers used in the study.

Table 5 Area ratios of five nozzle Mach numbers

Ma	1.25	1.5	1.75	2	2.25
A^*/A	1.05	1.18	1.39	1.69	2.10

A^*/A refers to outlet area/throat area

As shown in Fig. 13, as the Mach number of the top-blown oxygen lance nozzle increases, the jet velocity at the nozzle outlet increases. The length of the jet core zone formed by the Ma=1.25 nozzle is concise, and the velocity decays quickly. The jet quickly loses enough kinetic energy after being ejected from the nozzle. The airflow velocity inside the Ma=2.00 and Ma=2.25 nozzles is very high, reaching approximately 450−500 m/s. The jet velocity drops sharply after ejection from nozzle, forming a jet cavity. This is because the high-speed fluid ejected interacts with the surrounding fluid to form a high-speed vortex structure at the nozzle.

The rotation direction of the vortex is opposite to the jet direction, causing the fluid velocity to decrease and the pressure to increase near the nozzle. This forms a cavity in the center of the jet, namely, the jet cavity. Therefore, the jet formed by the Ma=1.50 and Ma=1.75 nozzles is more stable. The jet velocity is higher, and the core zone length is longer for the Ma=1.75 nozzle. This makes it a more suitable Mach number for the nozzle.
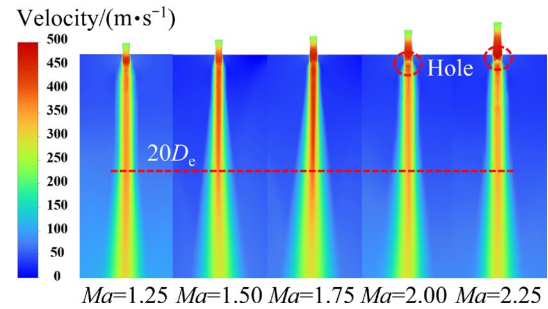

Fig. 13 Velocity contour maps of jet flow at different nozzle Mach numbers

The axial and transverse velocity distributions of the jet formed under different Mach numbers were analyzed to further investigate the influence of the Mach number on the jet characteristics of the top-blown oxygen lance nozzle. The results are shown in Fig. 14.

Figure 14(a) shows that the stability of the jet velocity on the axis is poor for the jets ejected from the Ma=2.00 and Ma=2.25 nozzles. The velocity decay is shifted when the jet moves within the range of $0-7D_e$ on the axis. Generally, the velocity variation of the jet formed by the Ma=1.25 nozzle is the smallest within $50D_e$. The velocity decay from $6D_e$ to $50D_e$ is slower than other nozzles. This indicates that jet velocity is relatively stable after ejection, and the resistance from the surrounding fluid is relatively small. The velocity variation of the top-blown jets ejected from the Ma=1.50 and Ma=1.75 nozzles is relatively regular, especially for the Ma=1.75 nozzle. The velocity decay curve of the jet first becomes gentle ($0-12D_e$) and then steep ($(12-40)D_e$). It finally tends to be gentle again ($(40-50)D_e$). Figure 14(b) illustrates that the diffusion of the jets at the cross-section of $20D_e$ is not significantly different among nozzles of different Mach numbers, with the radius of the jet stream changing between 0.06 and 0.08 m. Generally, the larger the Mach number is, the larger the radius of the jet stream is.
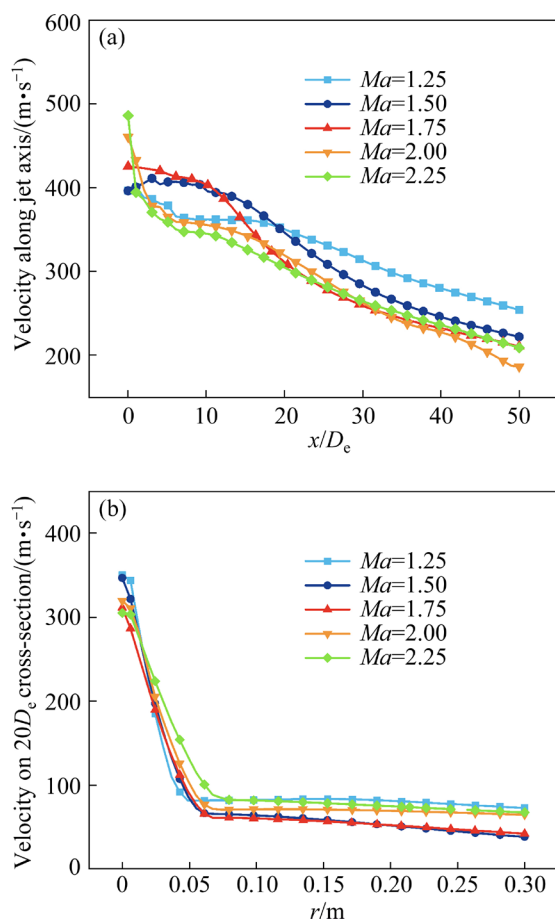
Fig. 14 Velocity distribution along jet axis (a) and on $20D_e$ cross-section (b) at different nozzle Mach numbers

4 Conclusions

(1) By comparing the computational results under different turbulence models, it is found that the standard k-ε model is more suitable. Compared with the simulation results of the jet core area length value, the error values are 2.72% and 6.18%, respectively. The simulation results are reliable.

(2) The airflow experiences continuous acceleration within the nozzle while density and pressure decrease upon exiting the nozzle and when losing the confinement of the duct, a high-speed jet is formed, which interacts with and entrains the surrounding gas downward. During the downward motion, the jet diameter increases while velocity and density decrease, leading to flow instability with the appearance of vortices, oscillations, and deflections. Eventually, the jet disperses gradually upon impacting the wall.

(3) Increasing the operating pressure for top blowing results in higher kinetic energy and slower jet decay, with little influence on the jet radius.

However, excessively high operating pressure can induce jet instability, affecting reaction uniformity and efficiency. The jet flow situation formed at the operating pressure of 0.6 MPa is optimal, where the maximum velocity of the jet is 456 m/s, and the center velocity and flow femoral width of the jet at $20D_e$ are 345 m/s and 0.124 m, respectively.

(4) As the Mach number of the nozzle increases, the jet velocity and diameter also increase. Excessive Mach numbers can lead to jet cavitation, while too low Mach numbers result in insufficient jet kinetic energy. The optimum nozzle Mach number is 1.75.

CRediT authorship contribution statement

Ai-liang CHEN: Supervision, Project administration, Writing – Review & editing, Funding acquisition, Conceptualization, Methodology; **Yao LIU:** Investigation, Writing – Review & editing, Visualization, Validation, Formal analysis, Investigation, Data curation; **Zi-biao WANG:** Investigation, Supervision, Writing − Review & editing, Data curation; **Huan-wu ZHAN:** Resources, Funding acquisition, Formal analysis; **Xue-xian JIANG:** Conceptualization, Supervision; **Feng-long SUN:** Conceptualization, Writing − Review & editing, Methodology; **Jiann-Yang HWANG:** Data curation, Project administration; **Xi-jun ZHANG:** Supervision, Project administration.

Declaration of competing interest

The authors declare that they have no known competing financial interests or personal relationships that could have appeared to influence the work reported in this paper.

References

[1] ZHOU Xiao-bin, ERSSON M, ZHONG Liang-cai, JÖNSSON P G. Numerical and physical simulations of a combined top-bottom-side blown converter [J]. Steel Research International, 2015, 86(11): 1328−1338.

[2] WANG Qin-meng, GUO Xue-yi, TIAN Qin-hua. Copper smelting mechanism in oxygen bottom-blown furnace [J].

Transactions of Nonferrous Metals Society of China, 2017, 27(4): 946−953.

[3] ZHAO Jin-xuan, WU Wei, ZHAO Bo, LI Xiang-chen, Xiao Feng. Influence of vanadium extraction converter process optimization on vanadium extraction effect [J]. Metals, 2022, 12(12): 2061.

[4] VISURI V V, JÄRVINEN M, KÄRNÄ A, SULASALMI P, HEIKKINEN E P. A mathematical model for reactions during top-blowing in the AOD process: Derivation of the model [J]. Metallurgical and Materials Transactions B, 2017, 48: 1850−1867.

[5] SABAH S, BROOKS G. Splash distribution in oxygen steelmaking [J]. Metallurgical and Materials Transactions B, 2014, 46: 863−872.

[6] WANG Jin-liang, CHEN Ya-zhou, ZHANG Wen-hai, ZHANG Chuan-fu. Furnace structure analysis for copper flash continuous smelting based on numerical simulation [J]. Transactions of Nonferrous Metals Society of China, 2013, 23(12): 3799−3807.

[7] SABAH S, BROOKS G. Study of cavity modes in BOF by analysis of sound [J]. Ironmaking & Steelmaking, 2016, 43(6): 473−480.

[8] LI Qiang, LI Ming-ming, KUANG Shi-Bo, ZOU Zong-shu. Numerical simulation of the interaction between supersonic oxygen jets and molten slag–metal bath in steelmaking BOF process [J]. Metallurgical and Materials Transactions B, 2015, 46: 1494−1509.

[9] DERING D, SWARTZ C, DOGAN N. Dynamic modeling and simulation of basic oxygen furnace (BOF) operation [J]. Processes, 2020, 8(4): 483.

[10] ZHANG Jing-shi, LOU Wen-tao, SHAO Pin, ZHU Miao-yong. Mathematical simulation of impact cavity and gas–liquid two-phase flow in top–bottom blown converter with eulerian-multifluid VOF model [J]. Metallurgical and Materials Transactions B, 2022, 53: 3585−3601.

[11] LI Qiang, LI Ming-ming, KUANG Shi-bo, Zou Zong-shu. Computational study on the behaviours of supersonic jets and their impingement onto molten liquid free surface in BOF steelmaking [J]. Canadian Metallurgical Quarterly, 2014, 53(3): 340−351.

[12] JIA Hong-bin, HAN Peng, LIU Kun, LI Yan-xin, FENG liang-hua. Jet characteristics of a double-structure oxygen lance and its interaction with the molten pool in BOF steelmaking [J]. AIP Advances, 2021, 11(8): 085330.

[13] YAO Liu-jie, ZHU Rong, TANG Yi-xing, WEI Guang-sheng, DONG Kai. Effect of furnace gas composition on characteristics of supersonic oxygen jets in the converter steelmaking process [J]. Materials (Basel), 2020, 13(15): 3353.

[14] DONG Peng-yuan, ZHENG Shu-guo, ZHU Miao-yong. Simulation and application of post-combustion oxygen lance in a top-blown converter [J]. Ironmaking & Steelmaking, 2023, 50(1): 55−66.

[15] CAO Ling-ling, LIU Qian, WANG Zhe, LI Na. Interaction behaviour between top blown jet and molten steel during BOF steelmaking process [J]. Ironmaking & Steelmaking, 2018, 45(3): 239−348.

[16] LI Jun, MA Zheng, CHEN Chao-yun, ZHANG Jie-yu, WANG Bo. Behavior of top-blown jet under a new cyclone

oxygen lance during BOF steelmaking process [J]. Processes, 2022, 10(3): 507.

[17] DONG Peng-yuan, ZHENG Shu-guo, ZHU Miao-yong. Research on nozzle design and application of single-flow postcombustion oxygen lance in a 120 t top-blown converter [J]. Steel Research International, 2021, 92(11): 2100203.

[18] ZHOU Jun, CHEN Zhou, ZHOU Ping, YU Jian-pin, LIU An-ming. Numerical simulation of flow characteristics in settler of flash furnace [J]. Transactions of Nonferrous Metals Society of China, 2012, 22(6): 1517−1525.

[19] LIU Fu-hai, ZHU Rong, WANG Qi-gang, BAI Rui-guo. Simulation and application of top lance with various tilt angles in dephosphorization Ladle Furnace [J]. ISIJ International, 2015, 55(8): 1633−1641.

[20] LIU Yang-wei, YAN Hao, LIU Ying-jie, LU Li-peng, LI Qiu-shi. Numerical study of corner separation in a linear compressor cascade using various turbulence models [J]. Chinese Journal of Aeronautics, 2016, 29(3): 639−652.

[21] YOON G H. Topology optimization for turbulent flow with Spalart–Allmaras model [J]. Computer Methods in Applied Mechanics and Engineering, 2016, 303: 288−311.

[22] LIU Yan-ting, YANG Tian-zu, CHEN Zhou, ZHU Zhen-yu, ZHANG Ling, HUANG Qing. Experiment and numerical simulation of two-phase flow in oxygen enriched side-blown furnace [J]. Transactions of Nonferrous Metals Society of China, 2020, 30(1): 249−258.

[23] YANG Tao, SUN Yan-hua, XU Liang, XI Lei, GAO Jian-min, LI Yun-long. Comparative study on flow and heat transfer characteristics of swirling impingement jet issuing from different nozzles [J]. International Journal of Thermal Sciences, 2023, 184: 107914.

[24] FAHEEM M, KHAN A, KUMAR R, KHAN S A. Experimental study of supersonic multiple jet flow field [C]//32nd International Symposium on Shock Waves. Singapore: Research Publishing Services, 2019: 2725−2731.

[25] ERSSON M, TILLIANDER A, JONSSON L. A mathematical model of an impinging air jet on a water surface [J]. ISIJ International, 2008, 48(4): 377−384.

[26] NGUYEN A V, EVANS G M. Computational fluid dynamics modelling of gas jets impinging onto liquid pools [J]. Applied Mathematical Modelling, 2006, 30(11): 1472−1484.

[27] ZHOU Xiao-bin, ERSSON M, ZHONG Liang-cai. Mathematical and physical simulation of a top blown converter [J]. Steel Research International, 2014, 85(2): 273−281.

[28] LIU Fu-hai, ZHU Rong, DONG Kai, HU Shao-yan. Effect of ambient and oxygen temperature on flow field characteristics of coherent jet [J]. Metallurgical and Materials Transactions B, 2015, 47: 228−243.

[29] MUÑOZ E D, BUCHLIN J M, MYRILLAS K, BERGER R. Numerical investigation of impinging gas jets onto deformable liquid layers [J]. Applied Mathematical Modelling, 2012, 36(6): 2687−2700.

[30] WANG Qin-meng, HUANG Ming-xing, YAN Shu-yang, WANG Song-song, TIAN Qing-hua, GUO Xue-yi. Hydrodynamic simulation of metal droplet settlement in molten slag [J]. Transactions of Nonferrous Metals Society of China, 2023, 33(4): 1244−1257.

[31] LOU Wen-tou, ZHU Miao-yong. Numerical simulation of

gas and liquid two-phase flow in gas-stirred systems based on Euler–Euler approach [J]. Metallurgical and Materials Transactions B, 2013, 44: 1251−1263.

[32] DONG Kai, ZHU Rong, GAO Wei, LIU Fu-hai. Simulation of three-phase flow and lance height effect on the cavity shape [J]. International Journal of Minerals, Metallurgy, and Materials, 2014, 21(6): 523−530.

[33] CAI Zhi-peng, XIE Yu-sheng, XIA An-wu. Effect of jet on molten pool in oxygen steelmaking process [J]. Steel, 1980(1): 14−19.

[34] HU Gui-dong, SONG Le-chen, ZHANG Cheng-gong, WU Feng-lin, YAO Yong-xing. Development of three-hole spray gun for oxygen top blown converter [J]. Journal of Peking University (Natural Society Edition), 1974(S1): 15−27.

[35] ZHANG Yan-chao, ZHANG Cai-jun, HAN Yang, WANG Bo, ZHU Li-guang. Jet characteristics of a high-Mach-number oxygen-lance nozzle under high oxygen pressure [J]. Metallurgical and Materials Transactions B, 2021, 52: 4070−4081.

[36] LI Ming-ming, LI Qiang, KUANG Shi-bo, ZOU Zong-shu. Determination of cavity dimensions induced by impingement of gas jets onto a liquid bath [J]. Metallurgical and Materials Transactions B, 2016, 47: 116−126.

[37] LIAN Wen-lei, CHANG Wei, XUAN Yin-min. Numerical investigation on flow and thermal features of a rotating heat pipe [J]. Applied Thermal Engineering, 2016, 101: 92−100.

[38] TAGO Y, HIGUCHI Y. Fluid flow analysis of jets from nozzles in top blown process [J]. ISIJ International, 2003, 43(2): 209−215.

[39] NAITO K I, OGAWA Y, INOMOTO T, KITAMURA S Y, YANO M. Characteristics of jets from top-blown lance in converter [J]. ISIJ International, 2000, 40(1): 23−30.

拉瓦尔喷管顶吹射流流动特性的湍流数值模拟

陈爱良 [1]，刘 瑶 [1]，王子彪 [1]，占焕武 [2]，蒋学先 [3]，孙丰龙 [1]，黄建阳 [4]，张希军 [5]

1. 中南大学 冶金与环境学院，长沙 410083；

2. 广西南国铜业有限公司，南丹 547204；

3. 桂林理工大学 南宁分校 冶金与资源工程学院，南宁 530001；

4. Department of Materials Science and Engineering, Michigan Technological University, Houghton, MI 49931, USA;

5. 金川集团股份有限公司 镍钴资源综合利用国家重点实验室，金昌 737100

摘　要：通过数值模拟研究了顶吹拉瓦尔喷管的湍流特性以及压力和马赫数对喷管的影响。结果与经验公式的误差为 2.72%，证实了结果的可靠性。结果表明，喷嘴内流体受管道结构的影响，导致压力和密度随速度的增加而降低。射流与周围气体之间的压力和速度差异会导致射流速度衰减、流股扩张、偏转和涡流。最佳顶吹压力为 0.6 MPa，最大射流速度为 456 m/s，在 $20D_e$(D_e 为喷管出口直径)时，射流中心速度为 345 m/s，射流宽度为 0.124 m。喷管最优马赫数为 1.75，最大射流速度为 451 m/s，$20D_e$ 时，射流中心速度为 338 m/s，宽度为 0.12 m。

关键词：顶吹射流；数值模拟；湍流；流动特性；拉瓦尔喷管

(Edited by Bing YANG)